First measurement in a magnetic confinement fusion experiment of the T + T → ^{5}He + n intermediate two-body resonant reaction

B. Eriksson[a,*], S. Conroy[a], G. Ericsson[a], J. Eriksson[a], A. Hjalmarsson[a], C. R. Brune[b], M. Gatu Johnson[c], M. Nocente[d], S. Fugazza[d], M. Rebai[e], JET contributors[f]

[a]*Department of Physics and Astronomy, Uppsala University, Lägerhyddsvägen 1, Uppsala, 752 37, Sweden*

[b]*Physics & Astronomy Department, 1 Ohio University, Clippinger Laboratories 251B, Athens, OH 45701, USA*

[c]*Plasma Science and Fusion Center, Massachusetts Institute of Technology, 167 Albany St., Cambridge, MA 02139, USA*

[d]*Department of Physics, University of Milano-Bicocca, Piazza della Scienza 3, Milan, 20126, Italy*

[e]*Institute for Plasma Science and Technology, National Research Council, Via R. Cozzi 53, Milan, 20125, Italy*

[f]*See the author list of "Overview of T and D-T results in JET with ITER-like wall" by CF Maggi et al. to be published in Nuclear Fusion Special Issue: Overview and Summary Papers from the 29th Fusion Energy Conference (London, UK, 16-21 October 2023*

Abstract

We report on the first experimental measurements made at a magnetic confinement fusion device of the T + T → α + 2n reaction indicating the presence of the intermediate two-body resonant reaction T + T → ^{5}He + n. During the second deuterium-tritium campaign (DTE2) at the Joint European Torus, measurements of fusion plasmas with high tritium concentrations, $n_T/(n_T + n_D) \approx 0.99$, heated with tritium neutral beam injection (NBI), were performed using the neutron time-of-flight (TOF) spectrometer TO-

*Corresponding author: benjamin.eriksson@physics.uu.se

FOR. We detect a peak in the neutron emission TOF spectrum consistent with the two-body resonant reaction. The TT neutron emission energy spectrum is modeled using an R-matrix framework where the distributions of the most likely model parameters given our experimental TOF data are determined utilizing a Markov chain Monte Carlo approach. We compare our best estimate of the TT neutron emission energy spectrum with results obtained at inertial confinement fusion experiments at the OMEGA facility and find a spectral shape that is consistent with the energy dependency in the neutron spectrum observed at OMEGA.

Keywords: keyword 1, keyword 2, keyword 3

1. Introduction

Two tritons (T) can fuse through the reaction, $T + T \rightarrow \alpha + 2n$. As a consequence of the three-body final state, the α and neutron energies create a broad energy spectrum with a lower limit of zero up to a maximum value given by the reaction kinematics. Further, there exists a resonant reaction occurring via an intermediate step, $T + T \rightarrow {}^5He + n$, where the ^{5}He is either in the ground or the first excited state. Due to the two-body intermediate state, the neutron and ^{5}He have well-defined energies which can be detected as a peak in the resulting energy spectrum as shown in [1, 2, 3]. Being able to properly model the TT neutron emission spectrum is important in the context of magnetic confinement fusion (MCF) and neutron spectroscopy for correctly estimating, e.g., the fusion fuel ion ratio [4] or the behavior and confinement of T ions [5] for tritium-dominated plasmas. Further, there exists a mirror reaction, $^3He + {}^3He \rightarrow \alpha + 2p$, which has an influence on the solar proton-proton chain. An energy dependency in the proton emission spectral shape may alter estimates of the ^{3}He + ^{3}He reaction rate at solar fusion energies [6].

Measurements of the neutron emission spectrum from the reaction have been performed at inertial confinement experiments, e.g. at the National Ignition Facility (NIF) [7]. Indications of an energy dependency in the reaction channel going via the ^{5}He ground state have been examined by Gatu Johnson et al. [6] where the neutron emission energy spectrum was measured at the OMEGA facility (Rochester, NY) by irradiating T_2 filled glass capsules with the OMEGA [8] system. In this paper, we report on the first experimental

measurements of the neutron emission energy spectrum from the T + T reaction in magnetically confined plasmas at the Joint European Torus (JET). Our findings reveal spectral features that are consistent with the energy dependency demonstrated at OMEGA.

2. Theoretical background

We utilize the same R-matrix model framework, described extensively in [9], as Gatu Johnson et al. to model the TT neutron emission energy spectrum. The model describes the reaction as sequential two-body decays involving the intermediate $\mathrm{T} + \mathrm{T} \rightarrow {}^{5}\mathrm{He} + \mathrm{n}$ state followed by ${}^{5}\mathrm{He} \rightarrow \alpha + \mathrm{n}$. Assuming an initial spin and parity $J^P = 0^+$, the model considers transitions to the intermediate state with orbital angular momenta $l = \{0, 1\}$ resulting in three partial waves $1/2^+$, $1/2^-$, and $3/2^-$. The $3/2^-$ and $1/2^-$ partial waves represent the ground state and first excited state of ${}^{5}\mathrm{He}$, respectively. As resonant states, they are anticipated to make a substantial contribution to the neutron emission spectrum. On the contrary, the $1/2^+$ partial wave is non-resonant and has been observed to contribute less to the neutron emission spectrum. Finally, di-neutron emission (nn) is considered in which the reaction occurs via the emission of an α-particle and two correlated neutrons. Examples of each contribution to the neutron energy spectrum are shown in figure 1 including the net interference between the various partial waves. In panel (a) the $1/2^-$, $3/2^-$, and di-neutron partial waves are shown in black, blue, and green, respectively. In panel (b) the $1/2^+$ partial wave and the net interference component are depicted in red and purple. The two (identical) orange lines in both panels depict the total TT neutron emission spectrum, resulting from the summation of the partial waves and interference component as presented in the two panels.

The partial wave amplitudes are set using what is referred to as feeding factors. One feeding factor is used for the di-neutron partial wave, here denoted A_{nn}. For the other partial waves a primary feeding factor, denoted $A^{(1)}_{J^P}$, and a secondary feeding factor, denoted $A^{(2)}_{J^P}$, are utilized resulting in a total of 7 feeding factors. The primary feeding factor determines the spectral shape of the neutron associated with the $\mathrm{T} + \mathrm{T} \rightarrow {}^{5}\mathrm{He} + \mathrm{n}$ reaction, whereas the secondary feeding factor is related to the neutron emitted in the subsequent ${}^{5}\mathrm{He} \rightarrow \alpha + \mathrm{n}$ decay. The effect of the primary and secondary feeding factors on the neutron energy spectrum is shown in figure 2 taken

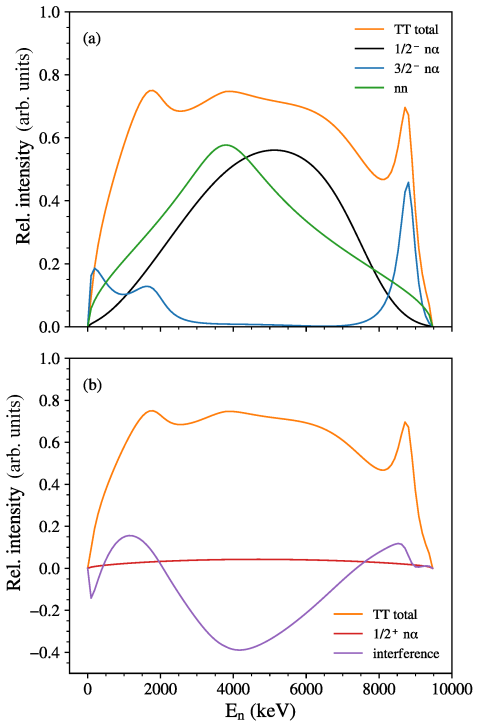

Figure 1: The total modeled TT neutron emission spectrum is shown as the orange line which is identical in both panels. The various components of the spectrum correspond to the reaction channels shown in panel (a) $1/2^-$ in black, $3/2^-$ in blue, di-neutron emission in green, and in panel (b) $1/2^+$ in red, and the net interference in purple.

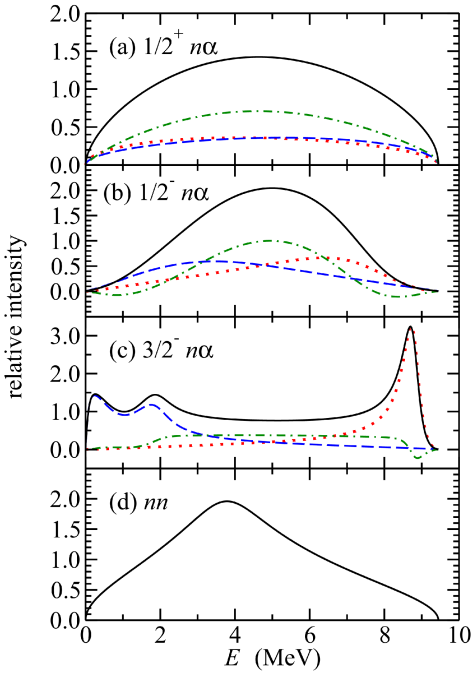

Figure 2: Neutron energy distributions for the partial waves, including the primary component (red dotted line), the secondary component (blue dashed line), the interference component (green dash-dotted line), and the total (black solid line). Only the total is shown for the nn case. Figure from [9].

from reference [9]. The description of the partial wave components from the same reference is repeated here for convenience:

> "$1/2^+$ nα: The particle spectra for this channel are rather featureless... [the neutron] spectra closely approximate elliptical energy distributions, characteristic of uniform phase space population.
>
> $1/2^-$ nα: The first excited state of ^{5}He gives rise to a broad peak in the primary neutron spectrum, while the secondary neutron spectrum is also broad, but peaks at a lower neutron energy. The effect of antisymmetrization is to make the overall spectrum narrower, with relatively little strength near the endpoints of the spectrum...
>
> $3/2^-$ nα: The ground state of ^{5}He gives rise to a narrow peak in the primary neutron spectrum near the maximum neutron energy. The secondary neutron spectrum shows a double-peaked feature below 2 MeV... which implies a strong tendency for the neutrons to be emitted in the same or opposite directions but not perpendicular to each other. Due to the recoil of the ^{5}He intermediate state, this correlation affects the secondary neutron energy distribution...
>
> nn: In this case, the neutron energy spectrum peaks just below 4 MeV and has considerably less strength near the endpoints compared to the $1/2^+$ nα channel, which has the same quantum numbers."

3. Methods

The JET machine has operated with high-concentration tritium plasmas, with tritium to deuterium (D) fuel densities on the order $n_{\mathrm{T}}/\left(n_{\mathrm{T}}+n_{\mathrm{D}}\right) \sim 0.99$, during the second deuterium-tritium campaign (DTE2) in 2021 and early 2022. The neutron time-of-flight spectrometer TOFOR [10, 11] acquired data throughout these experimental campaigns providing a large set of time-resolved data from which we can create TOF spectra to estimate the neutron emission energy distributions from each experimental discharge.[1] TOFOR utilizes a set of five plastic scintillation detectors (denoted S1) placed with a collimated line of sight passing through the core of the JET machine, followed by a secondary set of 32 plastic scintillators (denoted S2) at a distance of 1.2 m downstream of the S1 detectors, placed annularly around the sight line axis. By performing coincidence measurements between the S1 and S2 detectors, time-of-flight spectra can be calculated. The time-of-flight spectrum thus obtained can be related to the energy spectrum of the incoming neutrons since more energetic neutrons will give rise to coincidence events with shorter flight times, and vice versa.

In order to correctly interpret a given time-of-flight spectrum, it is necessary to have detailed knowledge of the response function of the instrument which relates the energy spectrum of incoming neutrons to the time-of-flight spectrum that these neutrons give rise to. For TOFOR, the response function has been determined using Monte Carlo calculations with the GEANT4 code [12]. Some key features of the response function are illustrated in figure 3, which shows the time-of-flight spectrum expected for mono-energetic neutrons of various energies, equally spaced in the interval 1.5-10.5 MeV. The figure shows that each neutron energy gives rise to a distinct, Gaussian-like peak centered around a well-defined time-of-flight value. Due to the inverse square relationship between energy and flight time, the peaks – despite being equally spaced in energy – become more narrowly spaced for shorter flight times. As a consequence, the resolution of TOFOR is better for lower neutron

[1] In this study, and within the context of JET, the term "experimental discharge" refers to the controlled confinement of a fusion plasma within the JET experimental setup. A discharge in this setting is a specific mode of operation under which the plasma has been studied, involving e.g., a given heating scheme, plasma density profile, temperature profile, fuel ion mixture, etc., under which the plasma is maintained. Typically, an experimental discharge at JET spans tens of seconds.

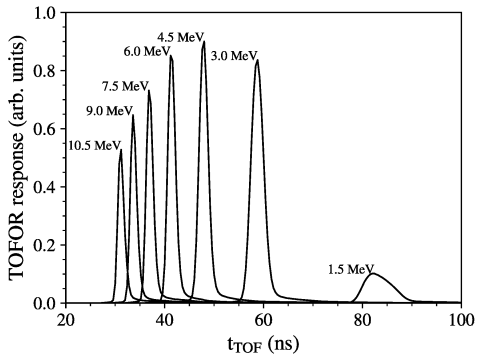

Figure 3: Simulated response of TOFOR to monoenergetic neutrons between 1.5 MeV and 10.5 MeV.

energies and gets gradually worse as the neutron energy increases. Furthermore, due to the design of the TOFOR instrument, which was optimized for DD operation, the detection efficiency is highest around 2.5 MeV and drops rapidly towards zero for neutron energies lower than ∼1.5 MeV. This effect is visible from the low intensity of the lowest energy peak in figure 3.

This section explains how we process and model the experimental TOF data. We begin by outlining the details surrounding the experimental discharges and the process of selecting data to create a summed TOF spectrum in section 3.1. Next, in section 3.2 we describe how we model the fuel tritium velocity distributions to determine the center-of-momentum (c.m.) energy, $E_{\text{c.m.}}$, for a given T + T reaction. Finally, in section 3.3, we discuss how we determine the model feeding factors using Markov chain Monte Carlo methods.

3.1. Experimental

To gather a large number of counts with TOFOR, we selected 90 experimental discharges from the tritium campaigns which utilized tritium neutral beam injection (NBI) [13, 14] to heat the tritium bulk plasma. The selected discharge numbers and time windows are given in Appendix A. The time windows for each TOFOR data set were chosen to coincide with the NBI heating phases (with the start and stop time provided by the NBI system) of the experimental discharges. The TOFOR data from the 90 discharges are summed to form the total spectrum shown in figure 4. Due to residual deuterium (D) in the machine from previous experiments, we expect to see signatures from the $\text{D} + \text{T} \rightarrow \alpha + \text{n}$ reaction, which produces 14 MeV

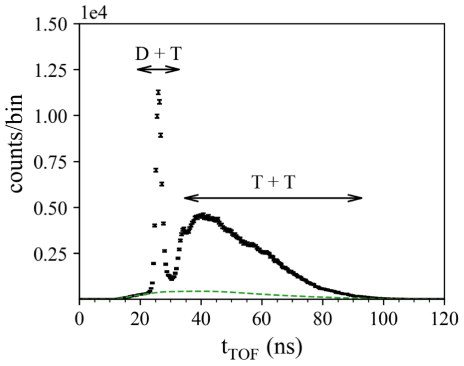

Figure 4: Experimental time-of-flight spectrum of the 90 summed discharges. The green dashed line corresponds to the estimate of the background due to random coincidences between the S1 and S2 detectors. A bin width of 0.4 ns is used.

neutrons, in addition to the neutrons produced by T + T reactions. As indicated by the black horizontal arrows, a peak due to 14 MeV DT neutrons is visible around $t_{\mathrm{TOF}} = 27$ ns, followed by the broad continuum between $30 < t_{\mathrm{TOF}} < 100$ ns produced by TT neutrons in the range 0-9.5 MeV. An estimate of the background, created by random coincidences between the S1 and S2 detectors, is included as the green dashed line using the methods described in [11, 15]. The data reduction techniques employed to produce the TOF spectrum are described in Appendix B. In addition to TOFOR, the neutron spectra from these discharges were also measured with two other spectrometers, based on single crystal, synthetic diamonds [16, 17]. The analysis of the data from these spectrometers is still ongoing, but the measurements have been seen to be broadly consistent with the TOFOR spectra presented here. A detailed analysis of the diamond spectrometer data will be the topic of a future publication.

3.2. Determining the effective $E_{c.m.}$ distribution

In addition to the various feeding factors, the R-matrix framework described in [9] requires the center-of-momentum energy, $E_{\mathrm{c.m.}}$, for the T + T system as an input parameter to calculate the neutron emission energy distribution. In our case, there is strictly speaking not one unique c.m. energy that describes all the reactants; rather, there is a distribution of c.m. energies that depends on the ion temperature and the slowing down distribution of the NBI ions. A proper calculation of the T + T neutron energy spectrum from the JET discharges considered in this paper should therefore consist of calculations of

spectra from a large number of c.m. energies, which should then be added together with weights proportional to the number of reactions expected from each respective c.m. energy. However, the R-matrix feeding factors – which are the basic parameters that we aim to determine from the TOFOR measurements – are also expected to vary with the c.m. energy, and it is not possible to determine this energy dependence from the available TOFOR data, since all data was collected from similar experimental conditions. We, therefore, follow the same approach as Gatu Johnson et al. [6] and determine an effective c.m. energy, representative of the T + T reactant distribution as a whole, and base all spectrum calculations off this single value of $E_{\mathrm{c.m.}}$.

In order to determine the c.m. energy distribution for the T + T system, we first need to model the tritium energy distributions present for the selected discharges. The primary contribution to the neutron emission spectrum comes from reactions between the thermal tritium population and a population of NBI tritons slowing down in the thermal plasma. The thermal tritium population is easily modeled using a Maxwell-Boltzmann distribution with an associated ion temperature T_{i}. Here, we make the approximation $T_{\mathrm{i}} = T_{\mathrm{e}}$, where T_{e} is the electron temperature, and use the high-resolution Thomson scattering (HRTS) system [18, 19] at JET to determine the average electron temperature for each experimental discharge time window. An example of the estimated energy distribution of the thermal tritium population for one experimental discharge is shown as the blue dashed line in figure 5. The approximation $T_{\mathrm{i}} = T_{\mathrm{e}}$ is valid in this work for three reasons. First, the approximation is generally valid for low-heating power scenarios (NBI power $\lesssim 15$ MW and neutron rates $\lesssim 10^{16}$ s^{-1}) [20], which the vast majority of the chosen discharges adhere to. Second, the subset of discharges for which T_{i} measurements are available from the charge exchange recombination spectrometer at JET [21, 22] confirms the similarity of the electron and ion temperature. Third, the few discharges in which the approximation may not hold will not affect the calculation of $E_{\mathrm{c.m.}}$ to a large degree. Indeed, performing a sensitivity test in which we increase the electron temperature by a factor 2 affects the calculated $E_{\mathrm{c.m.}}$ by less than 10%. Clearly, the center-of-momentum energy is dominated by the higher-energy NBI triton population. Next, the energy distribution of the NBI tritons is calculated using a Fokker-Planck equation [23] which describes the evolution of the NBI-injected tritons, for the given injection energy, slowing down in the thermal tritium plasma. The resulting NBI tritium distribution for the same discharge is shown in figure

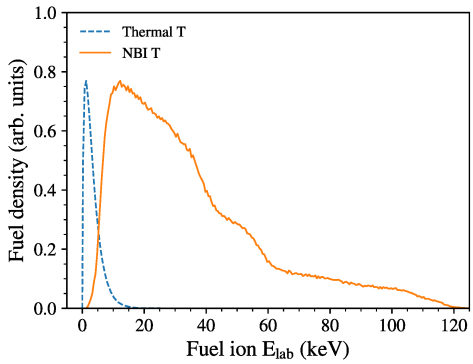

Figure 5: Fuel ion energy distributions normalized to the same peak value where the thermal tritium population (blue dashed line) is modeled as a Maxwell-Boltzmann distribution and the tritium NBI slowing down distribution is calculated using a Fokker-Planck equation.

5 as the orange line. We can now sample triton energies from the two distributions to create the c.m. energy distribution shown as the dashed black line in figure 6, again for the same discharge. Finally, since we only observe neutron-producing reactions, and the reaction rate is proportional to both the reaction cross section and the reactant relative speed, we need to weight the c.m. energy distribution by the product $\sigma(v)v$, where $\sigma(v)$ is the energy-dependent reaction cross section, and $v = |\mathbf{v}_2 - \mathbf{v}_1|$ is the relative T ion velocity of the T(T,2n)α reaction. σv is shown as the red dash-dotted line in the same figure. The product of the c.m. energy distribution and σv yields the final adjusted c.m. energy distribution shown as the solid black line. The process described above is repeated for all 90 discharges resulting in the black lines shown in figure 7. A weight is applied to each distribution in the figure to calculate the weighted average distribution shown as the orange solid line. The weights are calculated from the relative contribution of each experimental discharge to the measured TOF spectrum that is shown in figure 4. From the weighted distribution, we calculate the average effective c.m. energy, shown as the orange dashed line, to $E_{\mathrm{c.m.}} = 44.9$ keV with a standard deviation of 16.0 keV.

3.3. Parameter fitting

The four components shown in figure 8 are included in the model of the time-of-flight data. Three of these are constant throughout the fitting procedure, namely the background component due to random coincidences (green

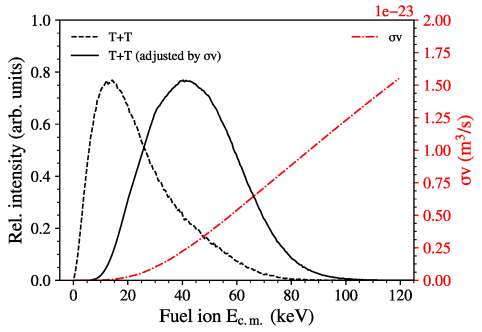

Figure 6: The black dashed line shows the center-of-momentum (c.m.) energy distribution of the T + T system for one experimental discharge where the interacting particle energies are sampled from the thermal and NBI populations shown in figure 5. The product of σv (red dash-dotted line) and the c.m. energy distribution yields the solid black line.

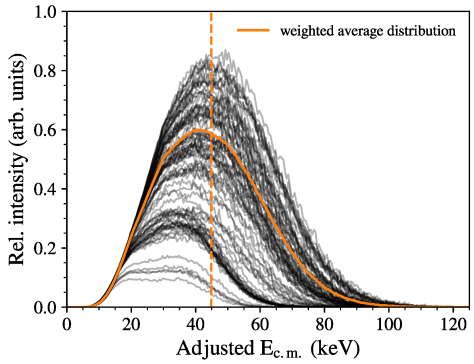

Figure 7: The black lines show the c.m. energy distributions of the T + T system adjusted by σv for each of the 90 experimental discharges. The weighted average distribution and its mean are shown as orange solid and dashed lines. The weights are given by the relative contribution of each discharge to the measured time-of-flight spectrum shown in figure 4.

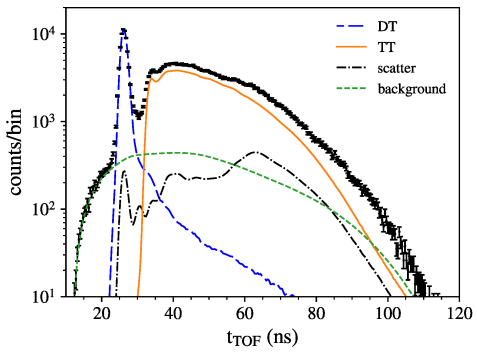

Figure 8: Components of the modeled time-of-flight spectrum, including the DT neutron emission peak (blue loosely dashed line), the broad TT neutron spectrum (orange line), the background due to random coincidences (green dashed line), and the contribution due to scattered neutrons (black dash-dotted line). A bin width of 0.4 ns is used.

dashed line), the DT peak (blue loosely dashed line), and the scatter component [24] (black dash-dotted line) which is calculated to estimate the contribution to the spectrum of neutrons scattering into the TOFOR sightline. An example of the modeled T + T reaction component is shown as the orange line in the same figure. The sum of the four components constitutes our best estimate of the modeled TOF spectrum. The scatter and DT component should in principle be calculated for each new fit to the data rather than being held constant. However, to save computation time it is calculated using an initial fit to the data deemed adequate for describing these components.

The neutron emission spectral shape from the T + T reaction is modeled using the seven feeding factors described in section 2. As is done in [6, 9], all parameters are allowed to vary except the $A^{(2)}_{1/2^+}$ channel which is set to zero. Consequently, the model has six free parameters which we vary to achieve the best fit to the TOF data. A Markov chain Monte Carlo algorithm [25] is utilized to perform a broad search of the parameter space. For each proposed sample of feeding factors, a TT neutron emission distribution is calculated and folded with the detector response function resulting in a modeled time-of-flight spectrum. The Cash statistic [26] is used as a figure of merit of the fit to the data. The analysis code is available in [27].

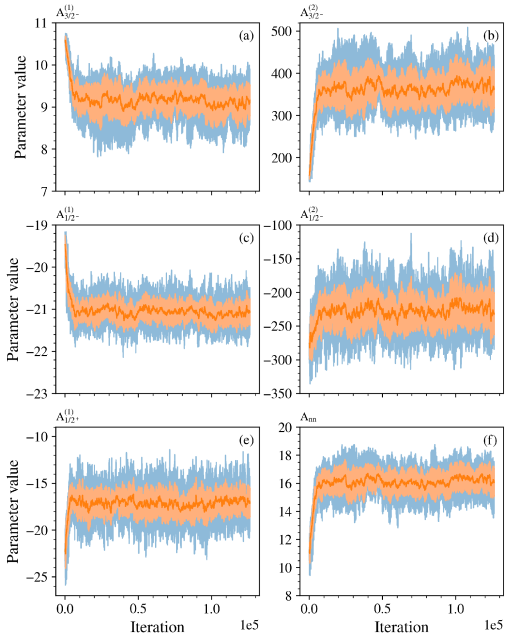

Figure 9: Sampled feeding factors in the Markov chain for (a) $A^{(1)}_{3/2^-}$, (b) $A^{(2)}_{3/2^-}$, (c) $A^{(1)}_{1/2^-}$, (d) $A^{(2)}_{1/2^-}$, (e) $A^{(1)}_{1/2^+}$, and (f) di-neutron emission. The stationary state of the Markov chain is achieved after approximately 20000 iterations. The samples are shown in blue, and the running average and running standard deviation are overlaid as the orange line and the orange band respectively.

4. Results

The accepted samples from the Markov chain are shown in blue in figure 9. The primary and secondary feeding factors $A^{(1)}_{3/2^-}$, $A^{(2)}_{3/2^-}$ and $A^{(1)}_{1/2^-}$, $A^{(2)}_{1/2^-}$ are shown in panels (a), (b) and (c), (d) respectively. The primary feeding factor $A^{(1)}_{1/2^+}$ and the di-neutron emission feeding factor, A_{nn}, are shown in panels (e) and (f). The running averages and standard deviations of the samples are overlaid as the orange line and band. The Markov chain reaches a steady state after approximately 20000 iterations. The samples from the steady state are selected and used to estimate the Markov chain stationary distributions shown in the diagonal of the corner plot in figure 10 as one-dimensional histograms for each feeding factor. The 50^{th} percentile (median) of each distribution is indicated by the black dashed line, and the gray shaded areas encompass the 16^{th} to 84^{th} percentiles of the distributions. The feeding factors determined in [6] for three average effective c.m. energies are included for comparison. These correspond to 18.5 keV (blue dash-dotted line), 45.1 keV (orange dotted line), and 58.6 keV (green loosely dashed line). For clarity, it is important to note that in the paper by Gatu Johnson et al., the stated values correspond to the peak values (in contrast to the averages) of the c.m. distribution, which are consequently lower there (16 keV, 36 keV, and 50 keV respectively). The off-diagonal figures are two-dimensional histograms indicating the covariance between the feeding factors. As an example, in the bottom row, the covariance between the A_{nn} and the remaining feeding factors is indicated. We observe a low covariance with the feeding factor $A^{(1)}_{1/2^+}$, as evident from the circular shape of the two-dimensional histogram. In contrast, we observe a high degree of covariance with the $A^{(1)}_{3/2^-}$ factor, indicated by the elliptical shape of the 2D histogram.

We randomly select 100 samples from the stationary distributions of the feeding factors (iterations $>$ 20000 in figure 9) and plot the corresponding total TOF models on top of our data. The result is shown in figure 11 which includes the same constant components displayed in figure 8. Here, we have zoomed in on the region dominated by TT neutrons. We find an excellent fit of the model to our data. The width of the line corresponding to the TT component (orange) and, as a consequence, the width of the total component (red), is a result of overlaying the 100 modeled TT emission spectra. The average neutron emission energy spectrum used to fit the data is shown as the black line in figure 12, the gray shaded area corresponds to the standard

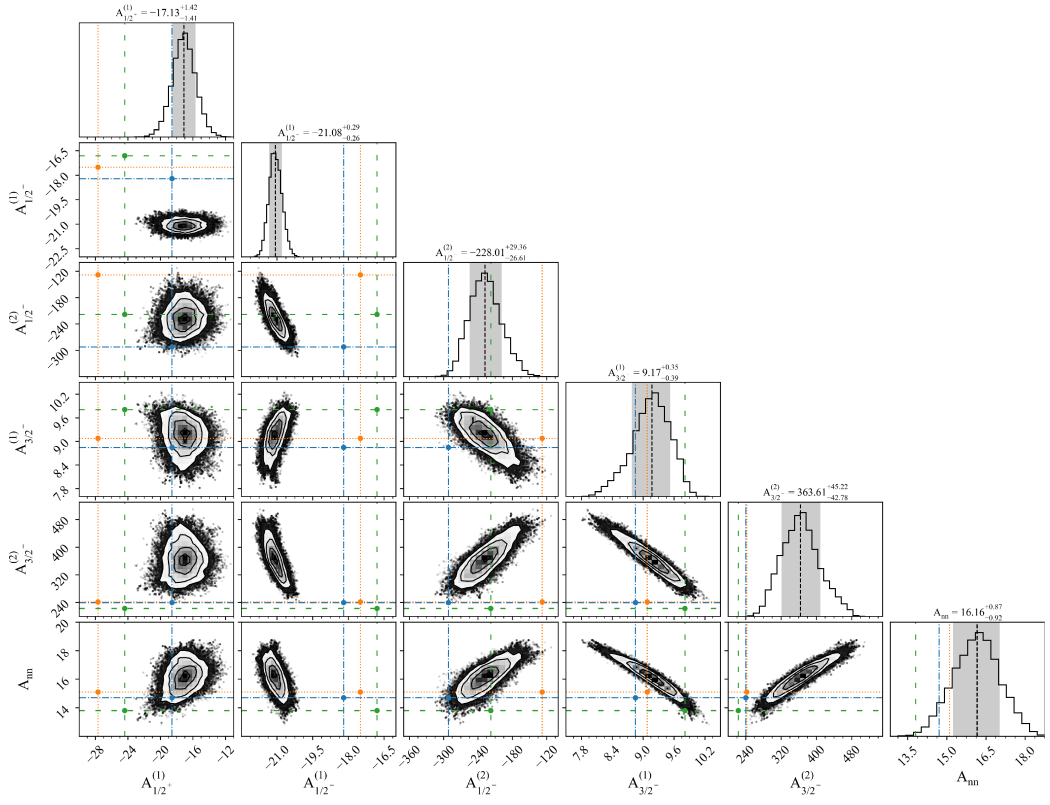

Figure 10: Corner plot showing the one-dimensional Markov chain stationary distributions of the feeding factors along the diagonal and the covariances between all feeding factors in the off-diagonal two-dimensional histograms. The parameter values determined by Gatu Johnson et al. are indicated in the figure for effective average c.m. energies 18.5 keV (blue dash-dotted line), 45.1 keV (orange dotted line), and 58.6 keV (green loosely dashed line).

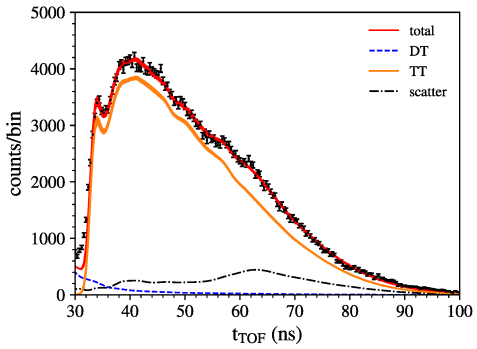

Figure 11: Total modeled time-of-flight spectrum (red line) overlaid on experimental data in the region dominated by TT neutrons, including the sub-components corresponding to TT neutrons (orange line), DT neutrons (blue loosely dashed line), and scattered neutrons (black dash-dotted line). The background due to random coincidences has been subtracted from the spectrum. A bin width of 0.4 ns is used.

deviation in each point. The neutron emission spectra modeled in the ex-

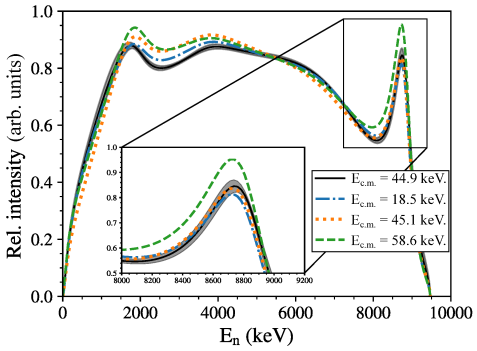

Figure 12: Modeled neutron emission spectrum (black line) corresponding to the average spectrum used in the fit to TOFOR data including the standard deviation (gray shaded area). Results from the OMEGA experiment [6] for three different c.m. energies are included.

periment at OMEGA [6] are illustrated in the figure by the blue dash-dotted, orange dotted, and green dashed lines with average effective c.m. energies of 18.5 keV, 45.1 keV, and 58.6 keV respectively. In concordance with the OMEGA paper, the neutron emission spectra are normalized between 4-6 MeV. The inset figure contains an enhanced display of the peak around 9 MeV produced mainly by the intermediate reaction going via the ^{5}He ground state, the strength of which is determined to a large degree by the $A^{(1)}_{3/2^-}$

feeding factor.

5. Conclusions and discussion

We have made the first measurements of the $T + T \rightarrow \alpha + 2n$ neutron energy spectrum at a magnetic confinement fusion device, showing the presence of the intermediate two-body resonant reaction $T + T \rightarrow {}^5He + n$. Measurements using the TOF spectrometer TOFOR were performed at the Joint European Torus for fusion plasmas with high fractions of tritium, $n_T/(n_T + n_D) \sim 0.99$, heated with tritium NBI. The neutron emission spectrum from reactions between two tritons is modeled using the R-matrix framework from [9]. The model effectively captures the spectral details in the TOF data, accurately fitting the peak associated with the intermediate reaction involving the ground state of helium-5 ($T + T \rightarrow {}^5He + n$). While the fitted spectrum agrees remarkably well with the TOFOR data across the entire time-of-flight range, it is important to note that TOFOR is virtually insensitive to neutrons with energies below approximately 1.5 MeV (see figure 3). Consequently, the region of the modeled neutron spectrum below this energy level should not be considered experimentally validated by the results presented in this paper.

As seen in figure 12, our best estimate of the modeled ground state peak intensity is consistent with the measurement made at a similar average effective c.m. energy (45.1 keV at OMEGA shown as the orange dotted line compared to our measurement at 44.9 keV shown as the black line). The consistency with the 45.1 keV measurement at OMEGA is further demonstrated in the one-dimensional histogram labeled $A^{(1)}_{3/2^-}$ in the fourth column in figure 10 by the proximity of the orange dotted line to our best estimate of the $A^{(1)}_{3/2^-}$ factor given by the black dashed line.

By utilizing a Markov chain Monte Carlo algorithm in this paper, we observe covariances between the feeding factors, e.g., an inverse correlation between $A^{(1)}_{3/2^-}$ and A_{nn}: increasing the intensity of the di-neutron partial wave results in a smaller value for $A^{(1)}_{3/2^-}$. This effect is demonstrated in figure 13 which shows the various partial wave components used to produce the total TT neutron emission spectrum for two samples selected from the Markov chain. The solid and dashed lines indicate the two selected sets of feeding factors. In panel (a) the $1/2^-$, $3/2^-$, and di-neutron partial waves are shown in black, blue, and green, respectively. In panel (b) the $1/2^+$ partial wave

and the interference component are depicted in red and purple. The orange lines in both panels depict the total TT neutron emission spectra, resulting from the summation of the partial waves and interference component as presented in the two panels. For the first set of feeding factors (indicated by the solid lines), A_{nn} is selected from the right-hand (high-value) side of the Markov Chain stationary distribution, whereas for the second set (indicated by the dashed lines) A_{nn} is selected from the left-hand (low-value) side of the distribution. The anti-correlation with the $A^{(1)}_{3/2^-}$ factor becomes apparent in the corresponding solid and dashed blue lines, where the large value of A_{nn} is compensated by a small value of $A^{(1)}_{3/2^-}$, and vice-versa. Further, the di-neutron partial wave is largely compensated by the interference component for the two cases in the area between 2-6 MeV, yielding similar total TT spectra for different values of A_{nn}.

It should be noted that the R-matrix model used in this paper calculates the TT neutron spectra in the center-of-momentum frame of the T + T system. In the JET experiments considered in this paper, the reactions were primarily of beam-target type, which means that the center-of-momentum frame does not coincide with the rest frame of TOFOR (where the spectrum is measured). Furthermore, the NBI tritons slowing down in the thermal tritium plasma conform to an anisotropic velocity distribution, which is expected to give rise to an anisotropy in the neutron emission energy spectrum. These effects might distort the spectrum shape somewhat, compared to the calculations presented in this paper. However, since the calculated spectra agree very well with the measured TOFOR data, any effects introduced by such anisotropic distributions are likely to be small but might introduce minor corrections to the best-fit feeding factors. This assumption is also supported by previous calculations [5], which indeed indicate that the use of NBI only has a minor effect on the shape of the neutron energy spectrum from the T + T reaction.

For future studies, it would be interesting to attempt to measure the low energy side of the T + T neutron spectrum in greater detail, since neither the TOFOR measurements presented in this paper nor the measurements in Gatu Johnson et al. [6] were sensitive to neutrons in this region. In particular, it would be interesting to investigate whether the peak-like structure around 1.5 MeV (caused primarily by the $3/2^-$ and the interference contributions (see figure 12) could be confirmed by measurements. Also, it would be interesting

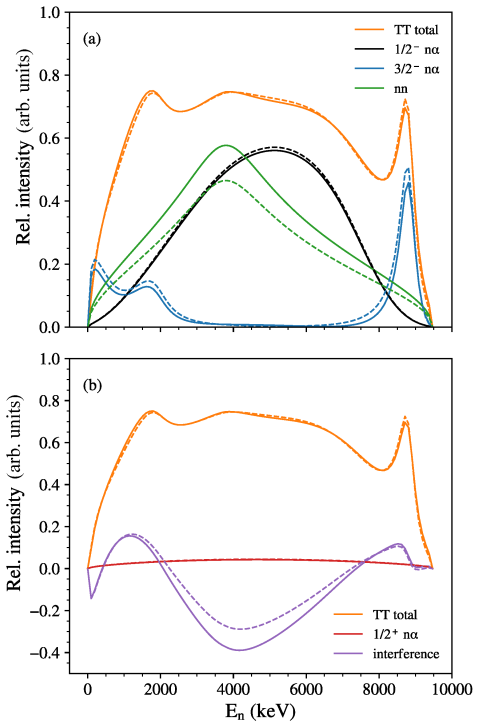

Figure 13: Two TT neutron emission spectra [orange lines in panels (a) and (b)], generated using two sets of feeding factors corresponding to the dashed and solid lines, including the various channel components and the interference contribution.

to perform measurements at even higher c.m. energies, to obtain further insight into the dependence of the spectral shape on the c.m. energy of the T + T system. However, it is unlikely that any of these investigations could be carried out at JET, both due to the inherent limitation of the TOFOR efficiency and due to the fact that JET will be decommissioned during 2024 and no more pure tritium plasmas are foreseen before then.

To conclude, our measurements of the TT neutron emission energy spectrum are consistent with the measurements made at OMEGA by Gatu Johnson et al. This provides further evidence of the energy dependency in the spectral shape, specifically in the intensity of the $A^{(1)}_{3/2^-}$ feeding factor, i.e., the peak around 8.5 MeV associated with the $3/2^-$ partial wave involving the ground state of ^{5}He.

Acknowledgement

This work has been carried out within the framework of the EUROfusion Consortium, funded by the European Union via the Euratom Research and Training Programme (Grant Agreement No 101052200 - EUROfusion). Views and opinions expressed are however those of the author(s) only and do not necessarily reflect those of the European Union or the European Commission. Neither the European Union nor the European Commission can be held responsible for them.

This work was supported by the U.S. Department of Energy, grants No. DE-FG02-88ER40387 and DE-NA0004065.

Appendix A. Table of experimental discharges

Table A.1 shows the list of experimental discharges with the corresponding JET pulse numbers (JPN) and time ranges used for the analysis of this paper. The discharges are selected using three selection criteria: i) the plasma is heated only through Ohmic heating and neutral beam injection of tritium, ii) the tritium concentration, $n_{\mathrm{T}}/(n_{\mathrm{T}} + n_{\mathrm{D}})$, as measured by the Penning gauge diagnostic KT5P at JET [28], is on average $> 99\%$ throughout the experimental discharge, and iii) the total neutron yield, as measured by the $^{235}\mathrm{U}/^{238}\mathrm{U}$ fission chambers, for the experimental discharge is $> 10^{14}$ neutrons. The discharges are selected from a set of experiments with varying plasma currents (ranging between 1.3-2.6 MA, with a majority around 2.3 MA), toroidal B-fields (ranging between 1.7-3.4 T, with a majority around 2.5 T), average NBI powers (ranging between 1-17 MW, with a majority around 10 MW), average electron temperatures (ranging between 1.5-3.5 keV, with a majority around 2.7 keV), and electron densities (evenly distributed between $4 \cdot 10^{19} - 8 \cdot 10^{19}$ m^{-3}).

Table A.1: JET time windows for the selected experimental discharges with the indicated JET pulse numbers (JPN) and times given in seconds.

JPN	t_0	t_1	JPN	t_0	t_1	JPN	t_0	t_1
98694	7.55	11.22	98986	6.29	12.92	99283	9.16	14.24
98695	13.10	18.96	98987	6.21	14.88	99288	10.13	15.96
98696	13.10	18.96	98990	6.23	12.88	100108	7.62	12.59
98697	7.56	13.11	98991	6.16	10.16	100110	10.13	15.96
98699	7.65	11.32	98992	6.18	12.10	100130	6.08	10.94
98788	7.55	12.01	98994	6.97	11.24	100131	6.06	10.96
98791	7.58	12.67	98995	7.08	13.82	100133	9.07	19.01
98792	10.05	12.09	98996	6.44	12.20	100134	9.08	17.99
98794	10.11	16.96	98997	6.30	10.64	100143	9.06	13.96
98795	10.10	17.75	98998	6.30	11.93	100164	7.28	21.68
98885	7.60	12.32	98999	6.35	8.55	100165	7.12	20.50
98891	7.59	12.43	99003	10.13	18.89	100166	7.16	21.40
98892	7.60	12.24	99137	7.59	11.12	100167	7.16	21.84
98906	12.44	20.83	99138	7.64	12.30	100168	7.14	19.47
98934	6.24	12.95	99140	6.12	14.93	100169	7.11	16.40
98935	6.02	6.93	99157	4.05	7.70	100170	7.16	21.84
98936	6.16	10.49	99159	4.03	5.99	100182	10.05	12.63
98937	6.14	11.09	99173	13.10	18.94	100186	10.09	15.95
98938	6.13	10.50	99182	7.07	13.75	100195	8.33	20.66
98939	6.32	11.06	99185	7.18	18.03	100196	8.33	20.66
98969	8.34	16.39	99187	6.04	9.36	100197	8.33	20.66
98975	6.01	6.50	99194	5.32	8.92	100198	8.30	18.67
98977	6.14	12.92	99208	7.55	8.82	100201	8.23	18.78
98978	6.22	12.74	99221	9.20	13.28	100202	8.29	20.70
98979	6.12	11.11	99223	4.02	5.43	100204	8.42	22.14
98980	6.07	11.26	99224	4.07	9.35	100205	8.29	20.53
98981	6.07	9.29	99225	4.07	8.75	100206	8.23	18.77
98983	6.13	12.28	99267	9.20	17.79	100225	15.34	23.92
98984	6.13	12.72	99269	9.14	14.84	100226	15.28	23.92
98985	6.18	12.80	99280	9.11	14.03	100227	15.28	23.93

Appendix B. Data reduction techniques

Panels (a) and (b) of figure B.14 show two-dimensional histograms for detector sets S1 and S2 respectively, with the electron equivalent (ee) energy deposited in the detector set on the vertical axis and the measured flight time on the horizontal axis. The main features of the two-dimensional histograms in panels (a) and (b) are now discussed. A gamma peak is visible around $t_{\mathrm{TOF}} = 4$ ns, the flight time of which is given by the distance between the S1 and S2 detectors and the constant speed of light. A peak due to 14 MeV DT neutrons is visible around $t_{\mathrm{TOF}} = 27$ ns, followed by the broad continuum between $30 < t_{\mathrm{TOF}} < 100$ ns produced by TT neutrons in the range 0-9.5 MeV. A smooth background, created by random coincidences between the S1 and S2 detectors, is visible across the full spectrum. The red lines in the top two panels are included to show the cuts applied to the data. The cuts are calculated by examining the kinematics associated with the maximal and minimal scattering angles given by the elastic, two-body (n-p) reaction in the plastic scintillators and the TOFOR geometry. In panel (a) there is an upper and lower kinematically allowed limit to the energy deposited in an S1 detector for a given flight time. In panel (b) there is, however, only an upper limit. Any event violating the limits set in panels (a) and (b) is discarded; the remaining events are projected onto the horizontal axis to form a TOF spectrum. Consequently, the resulting spectrum, shown in panel (c), is strongly background suppressed. A clear example of this can be seen in the absence of the gamma peak in the projected TOF spectrum. The background due to random coincidences which *does* adhere to the kinematic cuts in (a) and (b) can be estimated and included as a component when modeling the TOF spectrum; it is indicated in panel (c) as the green dashed line. Kinematic cuts and the random background estimate are fully described in [11]. The DT neutron peak and TT neutron continuum are indicated in panel (c) by the black, horizontal arrows.

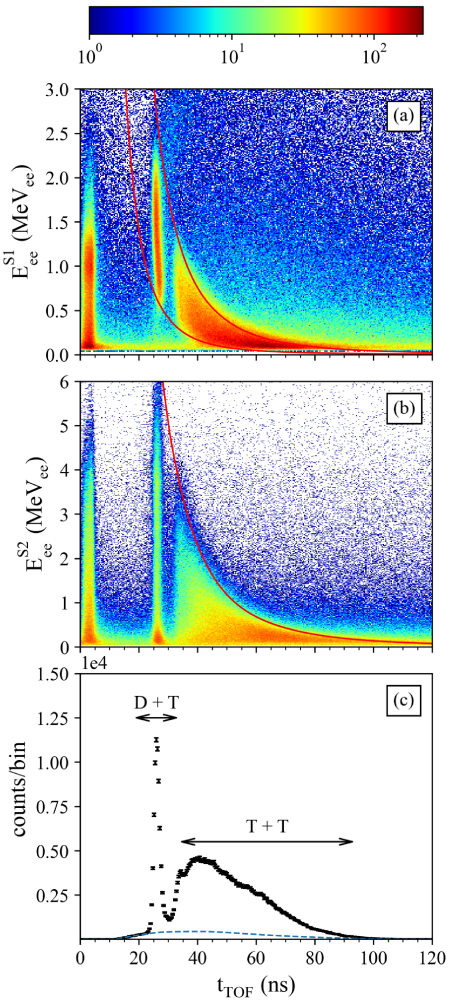

Figure B.14: 2D histograms of the 90 summed experimental discharges with the deposited energy on the vertical axis and flight time on the horizontal axis for (a) the S1 detectors, and (b) the S2 detectors. Kinematic cuts are shown as the red lines; any events between the lines in (a) and below the line in (b) are projected onto the horizontal axis in (c) to form a time-of-flight spectrum. The estimated background due to random coincidences is shown as the blue dashed line.

References

[1] K. Allen, E. Almqvist, J. Dewan, T. Pepper, J. Sanders, The T+T reactions, Physical Review 82 (2) (1951) 262.

[2] C. Wong, J. Anderson, J. McClure, Neutron spectrum from the T+T reaction, Nuclear Physics 71 (1) (1965) 106–112.

[3] D. Casey, J. Frenje, M. G. Johnson, M.-E. Manuel, N. Sinenian, A. Zylstra, F. Séguin, C. Li, R. Petrasso, V. Y. Glebov, et al., Measurements of the T(t, 2n)^{4}He Neutron Spectrum at Low Reactant Energies from Inertial Confinement Implosions, Physical review letters 109 (2) (2012) 025003.

[4] B. Eriksson, S. Conroy, G. Ericsson, J. Eriksson, A. Hjalmarsson, Z. Ghani, I. Carvalho, I. Jepu, E. Delabie, M. Maslov, et al., Determining the fuel ion ratio for D (T) and T (D) plasmas at JET using neutron time-of-flight spectrometry, Plasma Physics and Controlled Fusion 64 (5) (2022) 055008.

[5] J. Eriksson, C. Hellesen, S. Conroy, G. Ericsson, Neutron emission from a tritium rich fusion plasma: simulations in view of a possible future dt campaign at JET, in: 39th EPS Conference on Plasma Physics 2012, EPS 2012, 2-6 July 2012, Stockholm, Sweden, 2012.

[6] M. G. Johnson, C. Forrest, D. Sayre, A. Bacher, J.-L. Bourgade, C. Brune, J. Caggiano, D. Casey, J. Frenje, V. Y. Glebov, et al., Experimental Evidence of a Variant Neutron Spectrum from the T(t, 2n)α Reaction at Center-of-Mass Energies in the Range of 16–50 keV, Physical review letters 121 (4) (2018) 042501.

[7] D. B. Sayre, C. R. Brune, J. A. Caggiano, V. Glebov, R. Hatarik, A. Bacher, D. Bleuel, D. Casey, C. Cerjan, M. Eckart, et al., Measurement of the T+ T neutron spectrum using the national ignition facility, Physical Review Letters 111 (5) (2013) 052501.

[8] T. Boehly, D. Brown, R. Craxton, R. Keck, J. Knauer, J. Kelly, T. Kessler, S. Kumpan, S. Loucks, S. Letzring, et al., Initial performance results of the OMEGA laser system, Optics communications 133 (1-6) (1997) 495–506.

[9] C. Brune, J. Caggiano, D. Sayre, A. Bacher, G. Hale, M. Paris, R-matrix description of particle energy spectra produced by low-energy ^{3}H+^{3}H reactions, Physical Review C 92 (1) (2015) 014003.

[10] M. G. Johnson, L. Giacomelli, A. Hjalmarsson, J. Källne, M. Weiszflog, E. A. Sundén, S. Conroy, G. Ericsson, C. Hellesen, E. Ronchi, et al., The 2.5-MeV neutron time-of-flight spectrometer TOFOR for experiments at JET, Nuclear Instruments and Methods in Physics Research Section A: Accelerators, Spectrometers, Detectors and Associated Equipment 591 (2) (2008) 417–430.

[11] B. Eriksson, S. Conroy, G. Ericsson, J. Eriksson, A. Hjalmarsson, M. Weiszflog, Z. Ghani, M. Maslov, J. Contributors, TOFu: A fully digital data acquisition system upgrade for the neutron time-of-flight spectrometer TOFOR, Nuclear Instruments and Methods in Physics Research Section A: Accelerators, Spectrometers, Detectors and Associated Equipment 1049 (2023) 168126.

[12] S. Agostinelli, J. Allison, K. a. Amako, J. Apostolakis, H. Araujo, P. Arce, M. Asai, D. Axen, S. Banerjee, G. Barrand, et al., GEANT4—a simulation toolkit, Nuclear instruments and methods in physics research section A: Accelerators, Spectrometers, Detectors and Associated Equipment 506 (3) (2003) 250–303.

[13] G. Duesing, H. Altmann, H. Falter, A. Goede, R. Haange, R. Hemsworth, P. Kupschus, D. Stork, E. Thompson, Neutral beam injection system, Fusion Technology 11 (1) (1987) 163–202.

[14] D. King, R. Sharma, C. Challis, A. Bleasdale, E. Delabie, D. Douai, D. Keeling, E. Lerche, M. Lennholm, J. Mailloux, et al., Tritium neutral beam injection on jet: calibration and plasma measurements of stored energy, Nuclear Fusion 63 (11) (2023) 112005.

[15] M. Skiba, G. Ericsson, A. Hjalmarsson, C. Hellesen, S. Conroy, E. Andersson-Sundén, J. Eriksson, J. Contributors, Kinematic background discrimination methods using a fully digital data acquisition system for TOFOR, Nuclear Instruments and Methods in Physics Research Section A: Accelerators, Spectrometers, Detectors and Associated Equipment 838 (2016) 82–88.

[16] C. Cazzaniga, M. Nocente, M. Rebai, M. Tardocchi, P. Calvani, G. Croci, L. Giacomelli, M. Girolami, E. Griesmayer, G. Grosso, et al., A diamond based neutron spectrometer for diagnostics of deuterium-tritium fusion plasmas, Review of Scientific Instruments 85 (11) (2014).

[17] A. Muraro, L. Giacomelli, M. Nocente, M. Rebai, D. Rigamonti, F. Belli, P. Calvani, J. Figueiredo, M. Girolami, G. Gorini, et al., First neutron spectroscopy measurements with a pixelated diamond detector at JET, Review of Scientific Instruments 87 (11) (2016).

[18] R. Pasqualotto, P. Nielsen, C. Gowers, M. Beurskens, M. Kempenaars, T. Carlstrom, D. Johnson, J.-E. Contributors, High resolution Thomson scattering for joint European torus (JET), Review of Scientific Instruments 75 (10) (2004) 3891–3893.

[19] L. Frassinetti, M. Beurskens, R. Scannell, T. Osborne, J. Flanagan, M. Kempenaars, M. Maslov, R. Pasqualotto, M. Walsh, J.-E. Contributors, Spatial resolution of the JET Thomson scattering system, Review of Scientific Instruments 83 (1) (2012) 013506.

[20] H.-T. Kim, A. Sips, M. Romanelli, C. Challis, F. Rimini, L. Garzotti, E. Lerche, J. Buchanan, X. Yuan, S. Kaye, et al., High fusion performance at high Ti/Te in JET-ILW baseline plasmas with high NBI heating power and low gas puffing, Nuclear Fusion 58 (3) (2018) 036020.

[21] C. Negus, C. Giroud, A. Meigs, K.-D. Zastrow, D. Hillis, J.-E. Contributors, et al., Enhanced core charge exchange recombination spectroscopy system on Joint European Torus, Review of scientific instruments 77 (10) (2006).

[22] C. Giroud, A. Meigs, C. Negus, K.-D. Zastrow, T. Biewer, T. Versloot, J.-E. Contributors, et al., Impact of calibration technique on measurement accuracy for the JET core charge-exchange system, Review of Scientific Instruments 79 (10) (2008).

[23] T. H. Stix, Fast-wave heating of a two-component plasma, Nuclear Fusion 15 (5) (1975) 737.

[24] M. G. Johnson, S. Conroy, M. Cecconello, E. A. Sundén, G. Ericsson, M. Gherendi, C. Hellesen, A. Hjalmarsson, A. Murari, S. Popovichev,

et al., Modelling and TOFOR measurements of scattered neutrons at JET, Plasma Physics and Controlled Fusion 52 (8) (2010) 085002.

[25] D. Foreman-Mackey, D. W. Hogg, D. Lang, J. Goodman, emcee: the MCMC hammer, Publications of the Astronomical Society of the Pacific 125 (925) (2013) 306.

[26] W. Cash, Parameter estimation in astronomy through application of the likelihood ratio, Astrophysical Journal, Part 1, vol. 228, Mar. 15, 1979, p. 939-947. 228 (1979) 939–947.

[27] B. Eriksson, TT resonance analysis code, https://github.com/eriksson-benjamin/r_matrix (2023).

[28] D. Hillis, C. Klepper, M. Von Hellermann, J. Ehrenberg, K. Finken, G. Mank, Deuterium-tritium concentration measurements in the divertor of a tokamak via a modified penning gauge, Fusion engineering and design 34 (1997) 347–351.